Chapter 4
Fe-Zeolite Functionality, Durability, and Deactivation Mechanisms in the Selective Catalytic Reduction (SCR) of NO_x with Ammonia

Todd J. Toops, Josh A. Pihl and William P. Partridge

4.1 Introduction

Since the introduction of the first emissions control regulations in the 1970s and 1980s [1], catalysis has been implemented extensively to maintain compliance and to dramatically reduce the harmful pollutants emitted from combustion engines. For stoichiometric exhaust, primarily from gasoline-powered vehicles, precious metals, or platinum-group metals (PGM), such as Pt, Pd, and Rh, have been the hallmark of three-way catalysis, e.g., [2–4], as they are highly active in oxidation of carbon monoxide (CO) and hydrocarbons (HCs) as well as the reduction of nitrogen oxides (NO_x). The chemistry behind these reactions is equilibrium driven, as the more benign products of CO_2, H_2O, and N_2 are thermodynamically favored. However, these catalysts only function properly if the exhaust is at or near stoichiometric conditions. As a result, gasoline vehicle manufacturers began designing their engine control systems to operate with stoichiometric air/fuel ratios to optimize catalyst performance and minimize emissions. The need for more fuel-efficient vehicles, both with respect to increasing fuel costs and future CO_2 emissions regulations, is driving vehicle manufacturers to investigate more efficient combustion strategies, such as lean-burn gasoline, or increase production of more fuel efficient diesel vehicles.

Both diesel-powered vehicles (mobile source) and industrial plants (stationary source) operate primarily under lean exhaust conditions; i.e., excess oxygen content. This lean operation results in improved efficiency compared to stoichiometric operation, and these conditions are favorable for the oxidation of CO and HCs; however, it results in a very challenging environment for the catalytic reduction of NO_x. It is this challenge that the diesel community has been actively studying as the

T. J. Toops (✉) · J. A. Pihl · W. P. Partridge
Fuels, Engines and Emissions Research Center, Oak Ridge National Laboratory, 1 Bethel Valley Road, Oak Ridge, TN 37831, USA
e-mail: toopstj@ornl.gov

I. Nova and E. Tronconi (eds.), *Urea-SCR Technology for deNOx After Treatment of Diesel Exhausts*, Fundamental and Applied Catalysis,
DOI: 10.1007/978-1-4899-8071-7_4,

emissions regulations for these fuel-efficient vehicles have become more stringent [5]. Of the most common technologies for reducing NO_x from lean-burn engines—lean NO_x traps (LNT), hydrocarbon-based lean NO_x catalysis (LNC), and NH_3-based selective catalytic reduction (SCR)—SCR has had the most commercial success [6–18].

Industrial plants have been relying on a form of SCR since the 1960s [19], however, the controlled and stable nature of industrial plant operation allows several degrees of freedom that are not possible on a vehicle. Industrial plants have relatively steady emissions output, are able to introduce gaseous NH_3, can control the temperature of the catalyst to a very narrow window, and readily employ clean-up catalysts as the space constraints are not as limiting as on a vehicle. With these factors in mind, the low-cost vanadium and tungsten oxides supported on titania are the most widely used catalysts employed to selectively reduce NO_x from stationary sources [20]. These catalysts have also been implemented for diesel vehicles in Europe, but they have limited thermal durability as well as the potential to emit harmful gaseous vanadium [21–23].

The other catalysts that have found commercial success in SCR applications are zeolites exchanged with base metals, primarily Cu and Fe. These zeolite-based catalysts are particularly attractive because they do not rely on precious metals, have high tolerance to sulfur, and have good activity over a wide temperature range. Zeolites exchanged with Cu and Fe have been studied extensively, and much of the general chemistry and functionality is now known [24–28], although the detailed SCR mechanism is a matter of ongoing research [29–31]. These catalysts have improved hydrothermal stability over the previously discussed vanadia-based catalysts, and it is this improved durability that has led to the metal-exchanged zeolite being the predominant SCR system implemented in US-based commercial vehicles. However, durability is still a significant concern as several deactivation mechanisms are known to exist [17, 32–41]. A key limitation of many zeolites is their high temperature stability in the presence of steam. The SCR catalyst is exposed to high temperatures when the diesel particulate filter (DPF) required for particulate emissions control is regenerated and the trapped soot is oxidized at 600–700 °C. If uncontrolled, these thermal excursions, which are initiated over an upstream diesel oxidation catalyst (DOC), can lead to SCR catalyst degradation and loss of performance.

The primary difference between Fe- and Cu-exchanged zeolites lies in their respective operating windows for NO_x reduction: Fe-zeolites typically generate higher NO_x conversion efficiencies at higher temperatures, while Cu-zeolites work better at lower temperatures. This chapter will focus on Fe-exchanged zeolites; other chapters include detailed discussions of Cu-zeolites. Numerous zeolites have been studied for SCR applications, including MOR, FER, BEA, ZSM-5, CHA, SAPO-34 [24]. The zeolite structure and composition impact a variety of catalyst properties, including NO_x reduction activity, NH_3 storage capacity, and durability. Commercial systems have relied on zeolite beta (BEA) or one of the chabazite

structures (CHA or SAPO-34) due to their improved hydrothermal stability compared to other zeolites. Our prior work has focused on Fe-BEA samples provided by our industrial partners, so the discussions below will center on this class of materials.

This chapter will focus on the Fe-zeolite SCR system and will detail its functionality and durability and discuss the deactivation mechanisms that have been observed. The Cu-zeolite SCR system will be primarily discussed elsewhere in this book, but its reactivity and durability will be a source of comparison throughout.

4.2 Experimental Considerations in Evaluating and Aging Catalysts

Before fully delving into the functionality of the Fe-zeolite SCR catalysts, a brief discussion on experimental considerations is warranted. To meet vehicle emissions regulations, these catalysts must be fully functional under a wide range of 'conditions', expected exhaust temperatures, compositions, and flow rates that must be considered in the development and evaluation of these catalysts. However, before integration into a vehicle emissions control systems, catalysts are typically evaluated and aged in lab-scale environments. Much of this work is done in synthetic exhaust gas flow reactors; microreactors for catalyst powders and bench-scale flow reactors for monolithic core samples. Additionally, the catalysts are studied on engine dynamometer-based systems that more closely replicate on-road conditions, yet offer significantly more control over exhaust conditions than can be achieved in a vehicle. Results generated in each of these systems will be discussed here, with specific focus on bench-scale flow reactor studies.

Evaluation of core samples from commercial-intent catalysts has been an important method for measuring and predicting the behavior of on-board systems. Sample core sizes can vary from very small samples, 5–8 mm OD, to large samples, 75 mm OD, with most researchers focusing on samples around 25 mm OD and anywhere from 16 to 100 mm in length. Using washcoated catalyst cores allows the researcher to evaluate the system as close to its commercial application as possible, while maintaining control over temperature and gas composition. There can be challenges in obtaining a uniform washcoat distribution and sample-to-sample, or even channel-to-channel variations can be significant; however, if the sample is large enough and carefully harvested from the full size catalyst these variations can be minimized.

In focusing on SCR catalysts, it is important to first briefly define the chemistry that is important for the reduction of NO_x. There are three primary global reactions to consider:

- Standard SCR:

$$8NO + 8NH_3 + 2O_2 \rightarrow 8N_2 + 12H_2O \tag{4.1}$$

- Fast SCR:

$$4NO + 4NO_2 + 8NH_3 \rightarrow 8N_2 + 12H_2O \tag{4.2}$$

- NO_2 SCR:

$$6NO_2 + 8NH_3 \rightarrow 7N_2 + 12H_2O \tag{4.3}$$

Many of the elementary reactions involved in these global reactions are discussed elsewhere, including several of the side reactions leading to non-desirable products, e.g., N_2O [24, 42–44]. Other key chemical reactions that occur on these catalysts and impact performance are the following:

- NH_3 storage:

$$NH_3 + S \rightleftharpoons NH_3\text{–}S \tag{4.4}$$

- NH_3 oxidation:

$$3O_2 + 4NH_3 \rightarrow 2N_2 + 6H_2O \tag{4.5}$$

$$5O_2 + 4NH_3 \rightarrow 4NO + 6H_2O \tag{4.6}$$

- NO oxidation to NO_2:

$$O_2 + 2NO \rightleftharpoons 2NO_2 \tag{4.7}$$

It is with each of these reactions in mind that researchers probe the functionality of SCR catalysts with a goal of developing functional models that predict their behavior under a wide range of conditions.

To capture these processes in an efficient manner, experimental protocols are developed and employed. These typically rely on modelers and experimentalists working closely with each other to ensure that the protocol captures the key dynamics, and that the catalyst is in a well-known state before measuring reactivity. In SCR systems, this goes beyond de-greening or preconditioning, as the exchange metal can change oxidation states based on gas composition [27]. Two of these protocols will be introduced here. The first is a detailed approach that captures not only the key reactions but how reactivity changes at different NH_3 and NO ratios [45]. The second approach is more concise and only relies on four steps [46].

The detailed approach was developed to capture the key steady-state reactivity and the transient nature of SCR chemistry, specifically as it relates to NH_3 storage

capacity, NO_x reactivity with stored and gas-phase NH_3, and the influence of NH_3/NO_x and NO_2/NO_x ratios. The protocol was developed for implementation in an automated bench-scale flow reactor using core samples cut from commercial catalyst monoliths. The protocol includes steps to measure the following catalyst properties:

1. NH_3 storage capacity by three independent techniques:

a. NH_3 uptake during adsorption,
b. NH_3 release during isothermal and temperature programmed desorptions, and
c. NO_x reduction by *stored* NH_3, i.e., without NH_3 in the feed.

2. Steady-state SCR kinetics with varying reactant compositions:

a. NH_3/NO: 0.8, 0.9, 1.0, 1.1, 1.2,
b. NO_2/NO_x: 0.0, 0.25, 0.5, 0.7, 1.0,

3. NH_3 oxidation behavior, and
4. NO oxidation behavior.

The sequence of inlet gas compositions and how these changes in feed affect the effluent concentrations are shown in Fig. 4.1. Further analysis of these traces allows the calculation of steady-state conversions, NH_3 storage under three different conditions, as well as the stability of the stored NH_3. Data generated from selected portions of the protocol using Fe-zeolite SCR catalysts will be discussed in the following section for the following conditions: 150–550 °C, 60–120 k hr^{-1} GHSV, and a total NO_x feed of 150–450 ppm.

Another commonly referenced experimental approach is a 4-step protocol that aims to understand NH_3 capacity utilization in SCR catalysts by resolving three types of capacity: total, dynamic, and unused [46]. Total NH_3 capacity represents the equilibrium coverage if the entire catalyst was exposed to the inlet NH_3 concentration and temperature, i.e., in the absence of SCR reactions. This value generally increases with increasing NH_3 concentration and decreases with increasing temperature and is akin to an adsorption isotherm-based measurement. Dynamic NH_3 capacity is the NH_3 capacity used under SCR conditions; this value is a fraction of the total NH_3 capacity, has a constant value at steady-state SCR conditions, and is dynamic in the sense that it varies with transient SCR conditions. The unused or vacant NH_3 capacity is the difference between the total and dynamic NH_3 capacity, and represents unused capacity if the entire catalyst was at the inlet conditions. It should be clear that there is a balance between the sum of the dynamic and unused capacity, and the total capacity; i.e., the dynamic capacity cannot exceed the total capacity. In practice there are differences between the various capacities that vary with location, correlate with other SCR operating parameters, and give insights into capacity utilization.

The 4-step protocol is illustrated in Fig. 4.2 for a case using 200 ppm NO and NH_3 feed; of course other concentrations, NO_2/NO_x and NH_3/NO_x ratios would be needed to fully characterize the performance and properties of a given catalyst.

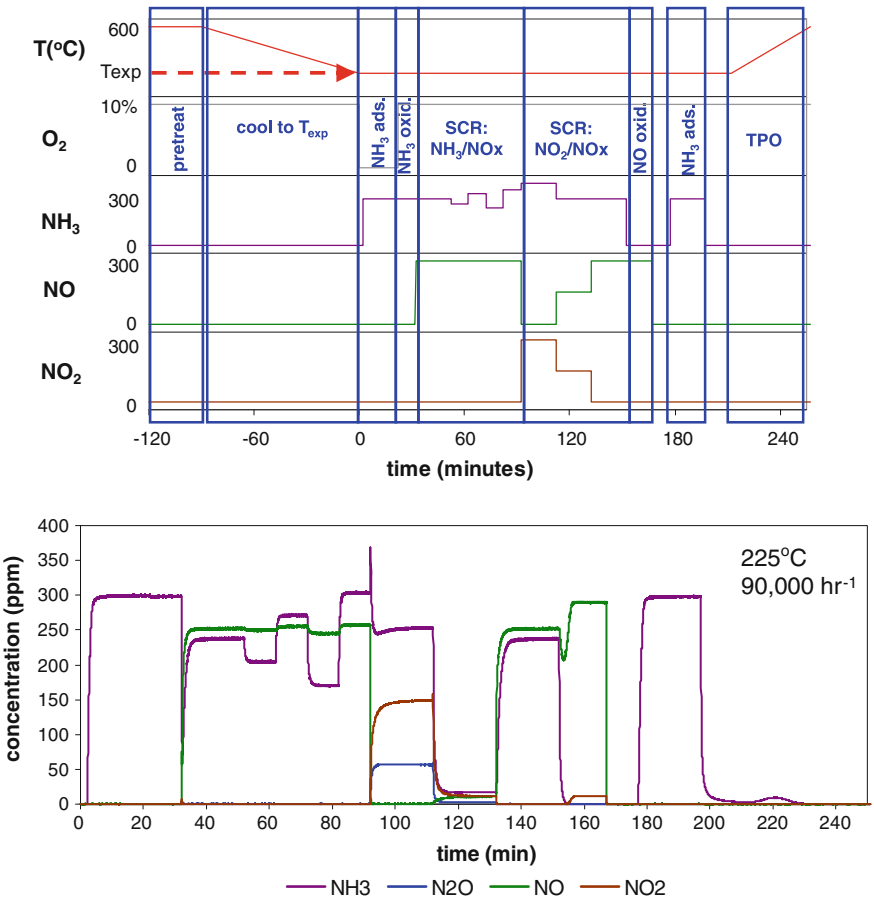

Fig. 4.1 Detailed SCR evaluation protocol with the feed sequence outlined on top (including the pretreatment) and an example effluent gas trace during the protocol of NH_3, N_2O, NO, and NO_2

Step 1 (200 ppm NO) is designed to fully clean the catalyst of stored NH_3, and quantify any NO oxidation. Step 2 continues the NO flow from step 1, but also introduces an equimolar flow of NH_3 and is used to measure transient and steady-state NO and NH_3 conversion and the dynamic NH_3 capacity during standard SCR operation. The area above the NO_x curve and below the NH_3 feed in step 2 (SCR in Fig. 4.2) represents the amount of NH_3 used for NO_x reduction, and the steady-state value is indicated by the green arrow. The area below the NH_3 curve represents the NH_3 slip, and the steady-state value is indicated by the orange arrow. Any difference between the steady-state NO_x and NH_3 curves represents NH_3 used for other reactions (e.g., NH_3 oxidation); these other reactions are assumed to be steady and continuous throughout the SCR step. The remaining step-2 area is the dynamic NH_3 capacity, which is determined by integrating between the NO_x and NH_3 curves and

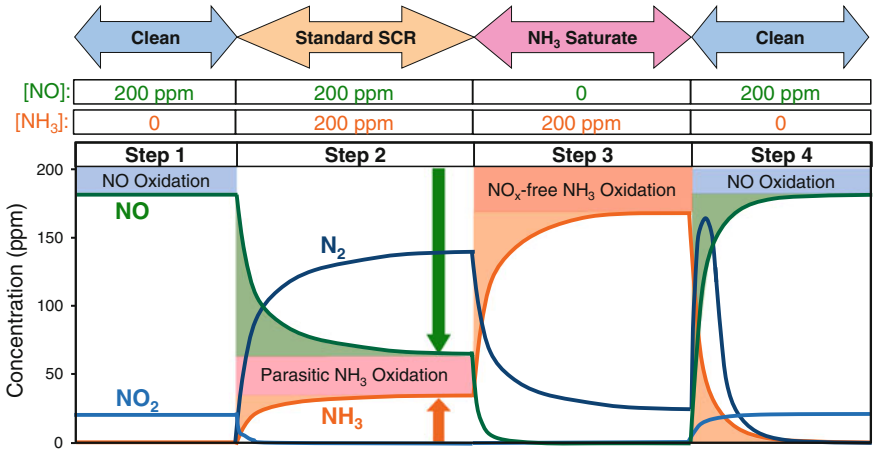

Fig. 4.2 4-step SCR evaluation protocol

subtracting the integrated NH_3 used for other reactions. Step 3 continues the NH_3 flow from step 2 at zero NO_x and is used to determine neat or NO_x–free NH_3 oxidation and the unused NH_3 capacity. It should be noted that NH_3 oxidation can differ in the presence and absence of NO, and specifically, can be enhanced by the presence of NO [13, 46–48]; these observations can be predicted and have been incorporated into SCR models [47, 49]. The unused NH_3 capacity is determined from integrating between the steady-state and instantaneous NH_3 curves, as indicated by the orange-shaded region in step 3 of Fig. 4.2. At the end of step 3 the total NH_3 capacity of the catalyst has been filled by sequentially filling the dynamic and unused capacity in steps 2 and 3, respectively; and the total NH_3 capacity can be independently measured in step 4 via its desorption and SCR reaction. Transitioning to step 4 the NH_3 flow is shut off and NO is reintroduced. The total NH_3 capacity is determined from the sum of the integrated NO_x reduction (green-shaded region in step 4 of Fig. 4.2) and the desorbed and unreacted NH_3 (orange-shaded region in step 4 of Fig. 4.2). Determining NH_3 capacity components from other protocols generally follows similar integrated analysis described here for the 4-step protocol.

Both of these protocols give a variety of parameters that are important in understanding the status and reactivity of a given catalyst. The detailed approach gives a more complete picture of more of the reactions, but it takes longer to run. The 4-step protocol targets the NH_3 storage behavior under specific conditions expected to occur in the vehicle and is more succinct, but lacks some the reactions necessary to develop a robust kinetic model. They are presented here to illustrate the range of approaches that can be taken in measuring the performance and properties of Fe-zeolite SCR catalysts, or other SCR catalysts for that matter. The remaining data will draw from results using both protocols.

4.3 Fe-Zeolite NO_x Reduction Characteristics

As discussed in the Introduction, Fe-zeolite SCR catalysts have similar properties to Cu-zeolites, but they do have distinct differences. To illustrate this, a protocol similar to the detailed one described above was used to evaluate Fe-and Cu-zeolite catalysts. Figure 4.3a shows the stoichiometric ($NH_3/NO_x = 1$) reactivity of both Fe- and Cu-zeolites when operated under standard SCR conditions ($NO_2/NO_x = 0$) at a space velocity of 30,000 h^{-1}. Significantly improved low-temperature reactivity of Cu is evident below 350 °C, and the high temperature benefits of Fe-zeolite are apparent above this temperature. Furthermore, the ability of Cu-zeolite to store high quantities of NH_3 are evident in Fig. 4.3b, c, where up to 4x more NH_3 is stored in the same volume of catalyst (note the different y-axis scales). As discussed above, both these catalysts were supplied by commercial partners and the precise zeolite framework and Si:Al ratios are not known. However, a consistent trend reported in the SCR literature has been that Fe-zeolites have less NH_3 storage than Cu-zeolites [28, 46]. One explanation that has been proposed is that the differences can be ascribed to the presence of NH_3 adsorption sites with different strengths on the two catalysts and/or to a different coverage dependence of the activation energy for ammonia desorption [28]. Another possibility is that the NH_3 can readily store on the Cu sites in addition to the zeolite framework, but not on the Fe sites. An additional feature of note in Fig. 4.3b, c is the difference between lean and rich storage. Both Cu- and Fe-zeolite store more under the rich storage conditions (NH_3 in the absence of O_2) compared to the lean case (NH_3 storage in the presence of O_2). A significant contributor to the difference between lean and rich storage is the NH_3 oxidation activity of the catalysts. Cu-zeolite, which is much more active for NH_3 oxidation, shows a larger difference between lean and rich storage at low temperatures compared to Fe-zeolite. This oxidation behavior will be addressed again later in this section.

While Fig. 4.3 illustrates the behavior of the SCR catalyst at the reactor outlet, it is often important to investigate the behavior of the reactants inside the catalyst to see how the NH_3 is being utilized and where the NO_x is being reduced. This distributed NH_3 utilization in an Fe-zeolite (BEA) SCR catalyst was studied using the 4-step protocol shown in Fig. 4.2. The partitioning of NH_3 utilization between NO_x reduction, slip, dynamic capacity, and other reactions (NH_3 decomposition or NH_3 oxidation by O_2) can be determined from step 2 (NH_3 + NO). Figure 4.4 shows how this utilization varies in the front half of the catalyst. The green arrows indicate the amount of NH_3 used for NO_x reduction (1:1 NH_3:NO stoichiometry) which is determined as the difference in the green curve and the 200-ppm feed value; this amount increases over the front half of the catalyst (0.5 L). The NH_3 slip (orange arrows) decreases along the catalyst axis, and NH_3 is fully consumed by the 0.5 L location; thus, with no remaining NH_3 slip there is no potential for further NH_3 storage or NO_x reduction. The other NH_3 reactions (light-blue boxes) are less at the catalyst front and approximately constant beyond the 0.25 L catalyst location. Figure 4.5 summarizes these results and shows the distribution of NH_3 utilization under steady-state SCR over the entire catalyst. Notably, 55–80 % of

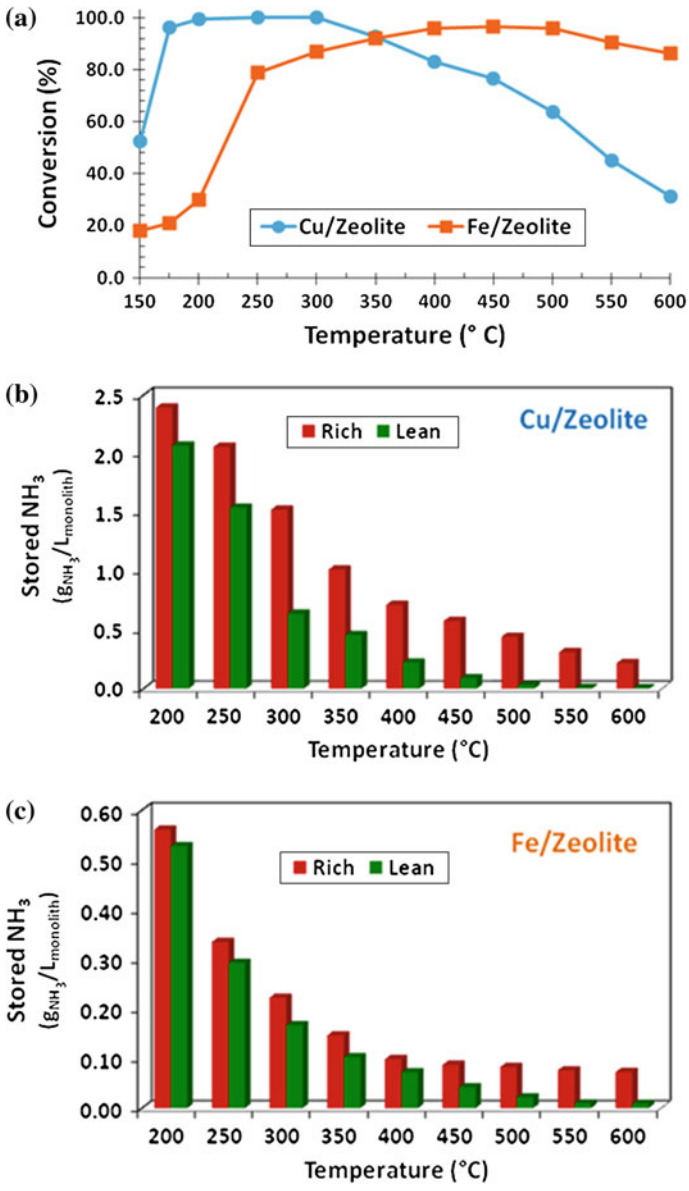

Fig. 4.3 **a** NO_x conversion comparison for Cu- and Fe-zeolite SCR catalysts; GHSV of 30,000 h^{-1} under 500 ppm NO, 500 ppm NH_3, 10 % O_2, 5 % H_2O, and 5 % CO_2. NH_3 storage under both lean (with O_2) and rich (no O_2) conditions for **b** Cu-zeolite and **c** Fe-zeolite; GHSV of 30,000 h^{-1}, 500 ppm NH_3, 0 or 10 % O_2, 5 % H_2O, and 5 % CO_2

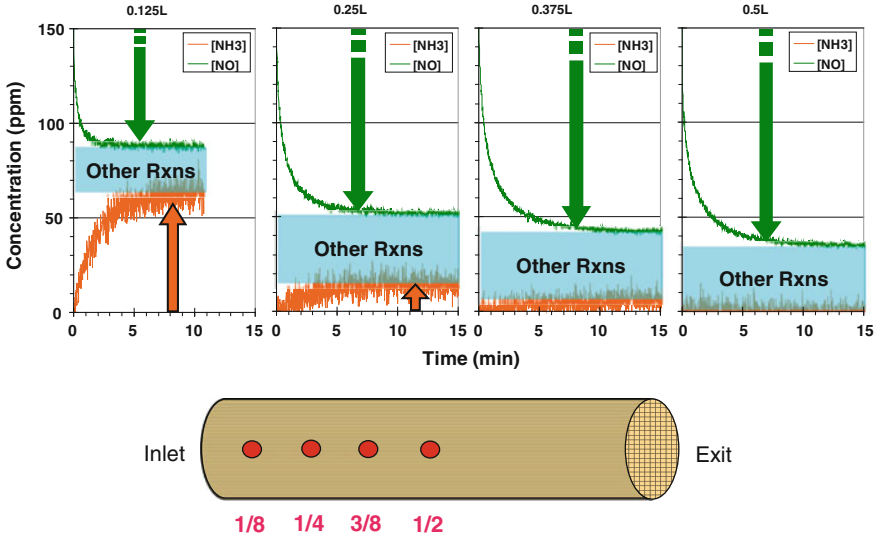

Fig. 4.4 Variation of NH_3 and NO concentrations in the front half of the Fe-zeolite catalyst during SCR reactivity. Space velocity of entire catalyst is 30,000 h^{-1} (GHSV); 200 ppm NO, 200 ppm NH_3, 10 % O_2, 5 % H_2O, 325 °C

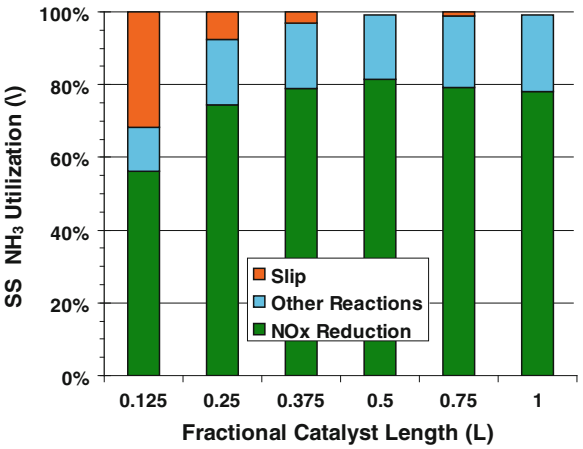

Fig. 4.5 Distributed NH_3 utilization throughout the Fe-zeolite SCR at steady state. Reaction conditions: 200 ppm NO, 200 ppm NH_3, 10 % O_2, 5 % H_2O, 325 °C, and GHSV = 30,000 h^{-1}

the NH_3 is used for NO_x reduction. However, a significant (15–20 %) amount of the NH_3 is consumed by other reactions and is not available for NO_x reduction use. Other results (not shown) indicate that the unused NH_3 capacity (step 3) increases linearly along the catalyst length, the dynamic NH_3 capacity (step 2) is concentrated in the front where SCR reactions occur, and the total capacity (step 4) balances with the dynamic and unused capacities. These types of catalyst insights improve kinetic and system models to design and control SCR catalysts for better efficiency and durability, e.g., how to reduce unwanted NH_3 oxidation by O_2.

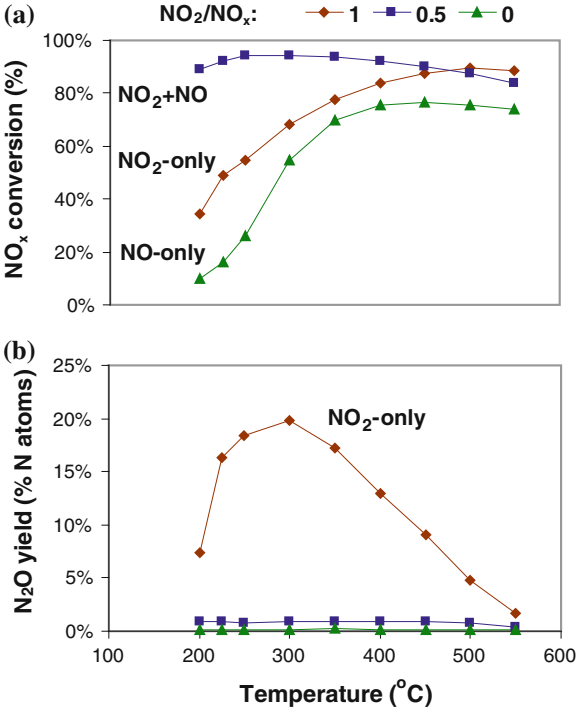

Fig. 4.6 SCR NO_x conversion and N_2O selectivity as a function of temperature for NO_2/NO_x ratios of 0.0, 0.5, and 1.0. Data collected with a fresh catalyst sample operated at a GHSV of 90,000 h^{-1} with stoichiometric quantities of NO_x (300 ppm NO, 150 ppm NO + 150 ppm NO_2, or 225 ppm NO_2, respectively), 10 % O_2, 5 % H_2O, and 5 % CO_2

As noted in Fig. 4.5, the NH_3 is consumed at approximately 0.375 L, or after ~1/3 of the catalyst at an SV of 30,000 h^{-1}. In studying the overall performance behavior, the data focused on this space velocity which is typical of vehicle applications. However, in implementing the protocols that do not rely on intra-catalyst measurements, higher space velocities, 90,000–120,000 h^{-1} are typically employed to measure reactivity with less than 100 % conversion of the reactants, i.e., NH_3 beyond 0.375 L in Fig. 4.4. Figures 4.6 and 4.7 are examples of the types of steady-state data that can be extracted from the protocol runs. Figure 4.6 shows the NO_x conversion activity of the Fe-zeolite SCR catalyst as a function of temperature for three NO_2/NO_x ratios (0.0, 0.5, and 1.0) over a de-greened catalyst. As expected for Fe-zeolite SCR catalysts, 1:1 mixtures of NO and NO_2 ("fast" SCR) yield much higher SCR reaction rates than NO or NO_2 alone [24]; however, for this Fe-zeolite formulation, NO_2-only is more reactive than NO alone. This appears to be a general characteristic of Fe-zeolites [24] and indicates that the "slow SCR" terminology used to describe NO_2 SCR is a misnomer. However, even though the overall NO_x reduction is improved with increasing NO_2 concentrations, the selectivity to the undesirable N_2O increases significantly for the NO_2-only case and measurably for the $NO_2/NO_x = 0.5$ case, as noted in the bottom graph in Fig. 4.6. This increase in N_2O formation is an indicator of the formation and decomposition of an ammonium nitrate intermediate rather than the more desirable ammonium nitrite [47, 49–51]. The NO_x conversions were measured at steady state (which can take hours to achieve

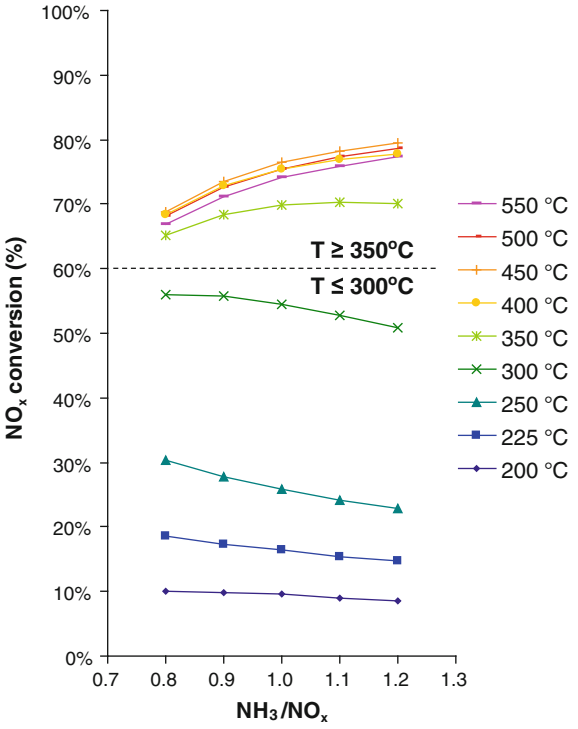

Fig. 4.7 SCR NO_x conversion as a function of NH_3/NO_x ratio at various operating temperatures. Data collected with a fresh catalyst sample operated at a GHSV of 90,000 h^{-1} under 300 ppm NO, 10 % O_2, 5 % H_2O, and 5 % CO_2

at these low temperatures), so no further accumulation of ammonium nitrate was occurring (the rates of formation and decomposition were equal). Thus, the higher NO_x conversions observed with NO_2 SCR are due to conversion of NO_2 to N_2 and N_2O and not accumulation of ammonium nitrate on the surface.

Figure 4.7 summarizes NO_x conversion as a function of NH_3/NO ratio and temperature. At 300 °C and below, the NO_x conversion decreases with increasing NH_3 dose. This behavior indicates that NH_3 inhibits the NO SCR reaction at low temperatures. Above 300 °C, the trend reverses, and NO_x conversion improves with increasing NH_3 concentration. Interestingly, Fig. 4.8 shows that NH_3 oxidation becomes measurable at temperatures above 300 °C. The maximum observed conversion is only 15 % at 550 °C, which is much lower than the reported values of >90 % on Cu-zeolites [52]. The lower NH_3 oxidation activity over the Fe-zeolite is the underlying reason for its higher NO_x conversion activity at high temperatures. Interestingly, the selectivity on these catalysts favors N_2 formation with only 2 % NO yield and <1 % N_2O at 500 °C. This is an important consideration since it illustrates that models need to account for losses of NH_3 to oxidation, but not necessarily more NO formation.

In addition to the steady-state data typically collected for evaluation of SCR catalysts, the test protocols include well-defined transient steps that generate additional insights into the catalyst surface chemistry. Figure 4.9 shows the NH_3

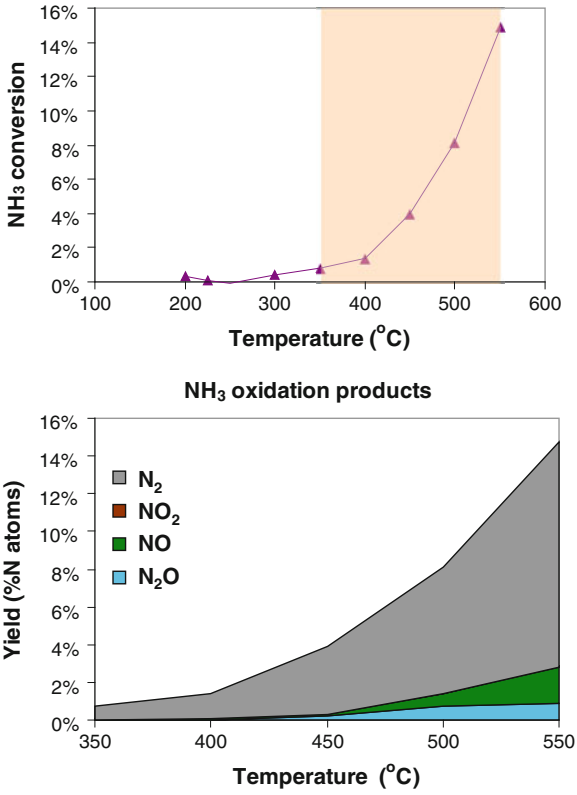

Fig. 4.8 NH_3 oxidation behavior (*top*) and its associated yield (*bottom*). Data collected with a fresh catalyst sample operated at a GHSV of 90,000 h^{-1} and a feed of 300 ppm NH_3, 10 % O_2, 5 % CO_2, 5 % H_2O

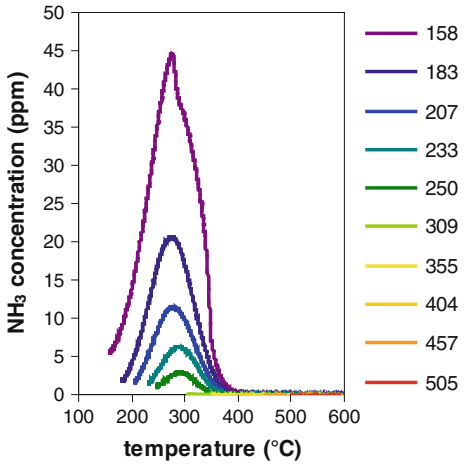

Fig. 4.9 Concentration of NH_3 released as a function of temperature during TPD portion of protocol. Data collected with a fresh catalyst sample operated at a GHSV of 120,000 h^{-1} under 300 ppm NO, 10 % O_2, 5 % H_2O, and 5 % CO_2

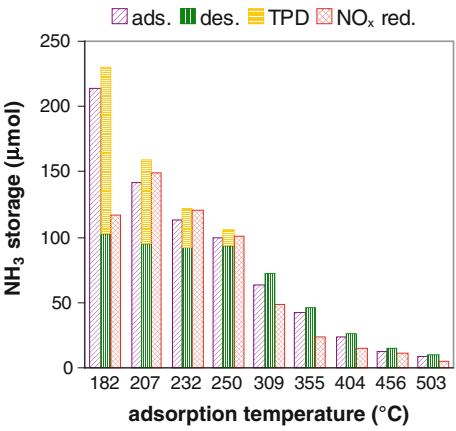

Fig. 4.10 Catalyst NH_3 storage capacity as a function of adsorption temperature as measured by uptake during adsorption (ads.), release during isothermal desorption (des.) and temperature programmed desorption (TPD), and NO_x converted by stored NH_3 after removing NH_3 from the feed gas (NO_x red.)

released from the catalyst during the temperature programmed desorption (TPD) at the end of the detailed protocol run. For adsorption temperatures above 300 °C, all of the NH_3 is released during the isothermal desorption step prior to the TPD (see Fig. 4.1). For adsorption temperatures below 300 °C, the amount of NH_3 desorbed during the TPD increases with decreasing adsorption temperature. For all but one of the TPD runs, there is a single NH_3 desorption feature centered at approximately 300 °C. Note that this temperature also represents the threshold for NH_3 inhibition of the NO SCR reaction. At 150 °C there is a second low temperature NH_3 desorption, likely due to formation of ammonium nitrates on the catalyst surface.

The detailed protocol includes several transient steps that provide independent measures of NH_3 storage capacity under various operating conditions. These include adsorption under inert conditions, isothermal, and temperature programmed desorption, and reactivity of NO with stored NH_3 after the NH_3 feed is shut off. Integrating the NH_3 stored, released, or reacted during each of these steps yields the capacities summarized in Fig. 4.10. The integrals from the two desorption steps are shown as stacked bars to indicate the total NH_3 desorbed. This plot yields two noteworthy insights. First, with the exception of the lowest temperature run, the three independent measurement techniques for determining storage capacities are fairly consistent. Based on this observation, we conclude that a measurement of NH_3 storage capacity can be achieved through any of the three techniques. The exception to this conclusion is for temperatures below 200 °C, where the slow SCR kinetics limit the NO_x reacted with stored NH_3. At these low temperatures, the appropriate measure of NH_3 storage capacity will depend on the application of the measurement. The consistency between the various NH_3 storage measurements is due to the low NH_3 oxidation activity of the catalyst. Catalysts with higher NH_3 oxidation rates (such as Cu-zeolites) exhibit much larger differences between NH_3 stored under inert conditions as compared to NH_3 desorbed/reacted under oxidizing conditions.

4.4 Durability, Aging Techniques, and Deactivation Mechanism Affecting Performance

Much of the research performed and publicly disseminated relies on fresh or degreened catalyst samples; however, aging can have a significant impact on the performance of these catalysts. It is critical to understand these impacts since vehicle emissions must be certified with the catalysts in an aged state. For light-duty vehicles this aged condition is 120,000–150,000 miles and for heavy-duty vehicles it is 435,000 miles. The primary factor that goes into aging is the thermal durability requirements, as the emissions control devices are expected to reach temperatures up to 800 °C under typical operating conditions. This high temperature is expected during the active regeneration of the DPF or under stoichiometric operation of lean gasoline engines. Additionally, reversible deactivation from hydrocarbons and sulfur can affect the SCR chemistry [32, 34, 39, 40], and there have been reports of irreversible contamination from metals originating from the fuel [53–56], lubricants [38], or even upstream catalysts [35–37]. Operating these catalyst systems to the end of full useful life, especially when evaluating several new catalysts and operating procedures, is often unreasonable and cost-prohibitive; therefore, accelerated aging protocols/routines are necessary. The remainder of this section will address the deactivation mechanisms observed in Fe-zeolite SCR catalysts as well as the accelerated aging protocols often used to produce the aged samples.

The majority of published research on the thermal durability of zeolite-based SCR catalysts utilize controlled furnace-based hydrothermal aging to accelerate the aging process [10, 57, 58]. This approach can adequately match the thermal strains that catalysts experience under engine or vehicle aging conditions, as has been elegantly demonstrated by Schmieg et al. on a Cu-zeolite (CHA) SCR catalyst [52]. An additional benefit of furnace aging is that it allows the isolation of thermal durability aspects of the catalyst. Generally, modern metal-exchanged zeolites have shown good durability under these controlled conditions, exhibiting less than a 10 % decrease in NO_x reduction activity. As an example, Fig. 4.11, shows the impact of aging an Fe-zeolite (BEA) SCR in the presence of H_2O, CO_2, O_2, and SO_2 in a furnace-based flow reactor for 64 h at 670 °C. As mentioned above, the NO_x conversion of the hydrothermally aged SCR catalyst was minimally affected. Devadas et al. obtained similar results after 50 h of hydrothermal aging with an Fe-zeolite (ZSM-5) SCR catalyst [57]. Even aged catalysts that maintain activity can experience a decrease in surface area and dealumination, which occurs when the Al^{3+} ions in the SiO_2–Al_2O_3 tetrahedral framework migrate out of the structure. This typically manifests itself as a decrease in NH_3 adsorption capacity and the loss of surface acidity [52, 59]. When aging above the mild temperatures shown in Fig. 4.11, i.e., >800 °C, many of the zeolites begin to dramatically breakdown structurally [52, 59].

For a more complete system-based durability evaluation, it is common to include the DOC and DPF in the aging protocol, and to rely on HC oxidation over

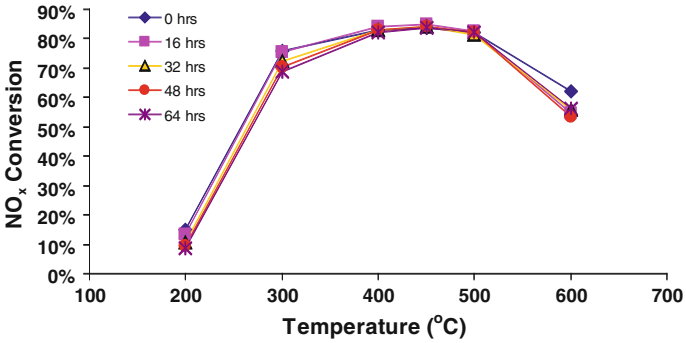

Fig. 4.11 Effect of aging time at 670 °C on NO_x conversion with Fe-zeolite SCR; evaluated with 5 % CO_2, 5 % H_2O, 14 % O_2, 350 ppm NO, 350 ppm NH_3, N_2 balance, GHSV = 30,000 h^{-1}

the DOC to generate the exotherm for inducing thermal aging. These approaches generally rely on engine-based systems, but in some instances could be performed with only flow reactors [60]. These more complex approaches can lead to several deactivation mechanisms occurring simultaneously, but can offer good insight into the potential limitations of the overall system. To illustrate this approach, an engine-based DOC-SCR-DPF accelerated aging approach will be discussed [37]. In the study, the aging of the SCR catalyst was achieved by increasing the exhaust temperature to replicate periodic DPF regenerations with target exhaust gas temperatures of 650, 750, and 850 °C at the SCR inlet. The activity of the engine-aged Fe-zeolite (BEA) SCR catalysts was then evaluated in a flow reactor to determine the extent of catalyst degradation, and material characterization was performed to ascertain the deactivation mechanisms associated with engine aging.

In implementing this engine and flow reactor systematic approach, it is possible to investigate different sections of the catalyst. Figure 4.12 shows the impact of aging temperature on the front and rear sections of the Fe-zeolite SCR catalysts. Very different activity is observed in these samples. Although there was an axial temperature gradient across the catalysts, ~100 °C when aging at 650 and 750 °C and ~50 °C at 850 °C, this cannot explain the dramatic difference in performance;. the rear of the 750 °C-aged SCR reached 650 °C, but it outperforms the front of the 650 °C-aged SCR. More evidence of involvement of a different deactivation mechanism can be seen in BET-measured surface areas in Fig. 4.13. The front and rear sections of the SCR catalyst engine aged at 650 °C are 60 m^2/g and 59 m^2/g, respectively, which both approximate the fresh catalyst, 58 m^2/g. At higher aging temperatures, surface areas begin to decrease and the thermal gradient is apparent as the front section is more adversely affected than the rear sample. Of course for this to be the sole cause of performance degradation there would have to be a notable surface area decrease in the front section of the sample aged at 650 °C to explain the results in Fig. 4.12. In examining the 850 °C results it is clear that both the front and rear sections have both significant activity losses and surface area losses.

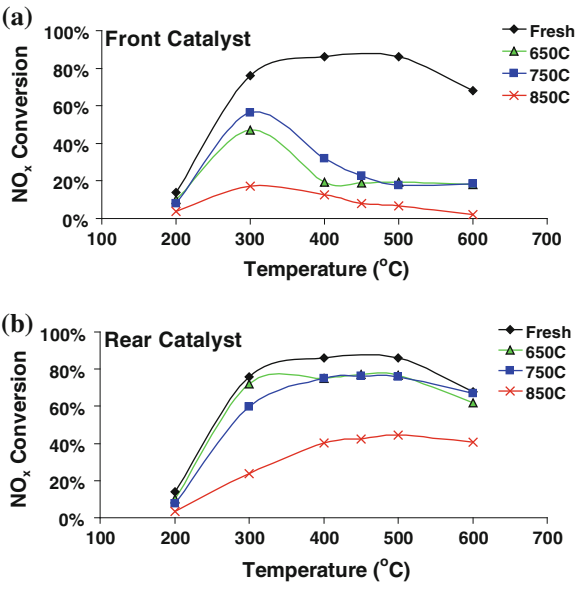

Fig. 4.12 NO_x conversion of the accelerated engine-aged Fe-zeolite SCR catalysts **a** front and **b** rear sections; evaluated with 5 % CO_2, 5 % H_2O, 14 % O_2, 350 ppm NO, 350 ppm NH_3, N_2 balance, GHSV = 30,000 h^{-1}

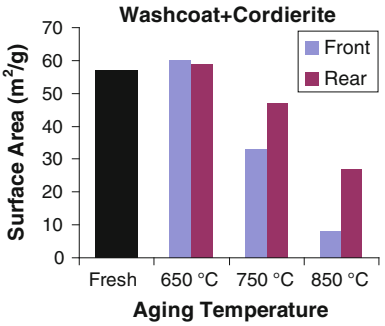

Fig. 4.13 BET surface area measurements of fresh and accelerated engine-aged Fe-zeolite SCR catalysts

The thermal aging effect on the zeolite structure is further evident in XRD and NMR studies shown in Figs. 4.14, 4.15, and 4.16. Figure 4.14 shows the XRD patterns of the fresh and accelerated engine-aged Fe-SCR catalysts; only the front sections are shown here. The clearest phase change that occurs is the gradual loss in the zeolite crystallinity at increasing aging temperatures. The primary zeolite peaks are visible at $2\theta = 8$ and 22.5°. The peaks are clear and predominant in the fresh sample, and also after aging at 650 °C. However, upon heating to 750 and 850 °C, the zeolite structure begins to diminish. This breakdown of the zeolite generally results in alumina formation with detectable peaks of alumina in the XRD patterns occurring at $2\theta = 43$ and 67°. These peaks are more discernible at 850 °C and to a lesser extent at 750 °C. Additionally, at higher aging temperatures, there is a minor growth in the Fe_2O_3 phase at $2\theta = 36$ and 54°. This indicates that active Fe cations in the fresh catalyst have formed Fe_2O_3 clusters in

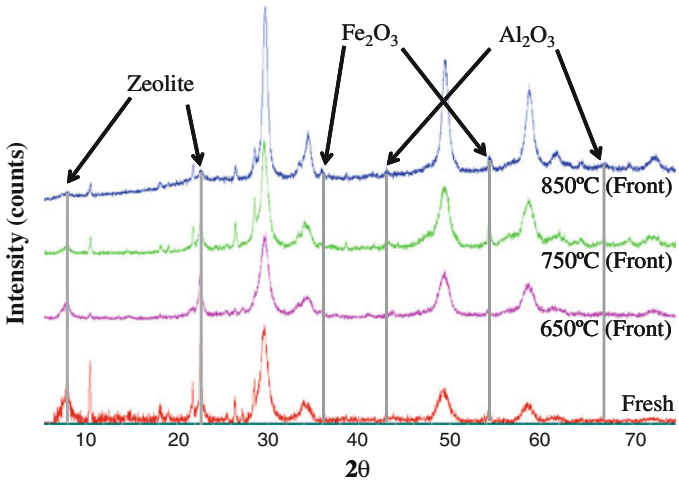

Fig. 4.14 X-ray diffraction patterns of fresh and accelerated engine-aged Fe-zeolite SCR catalysts

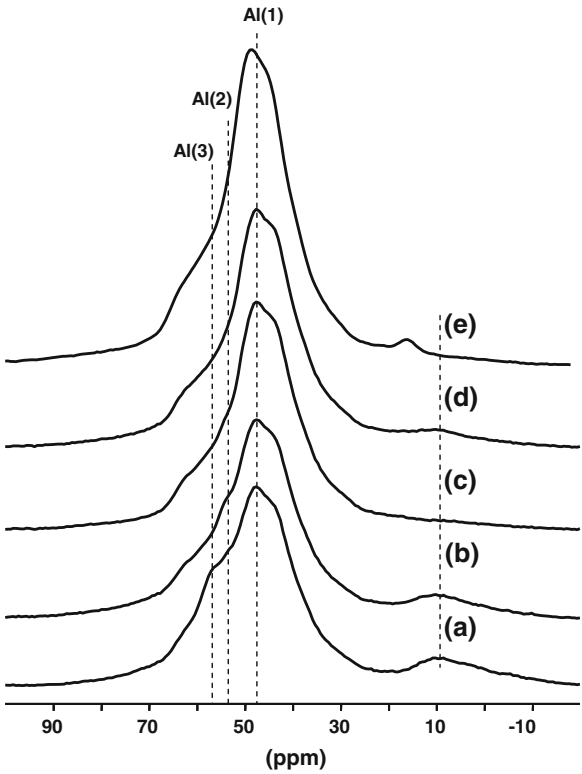

Fig. 4.15 One-dimensional ^{27}Al MAS spectra of the **a** fresh Fe-zeolite/cordierite, samples aged at **b** 650, **c** 750, and **d** 850 °C, and **e** cordierite

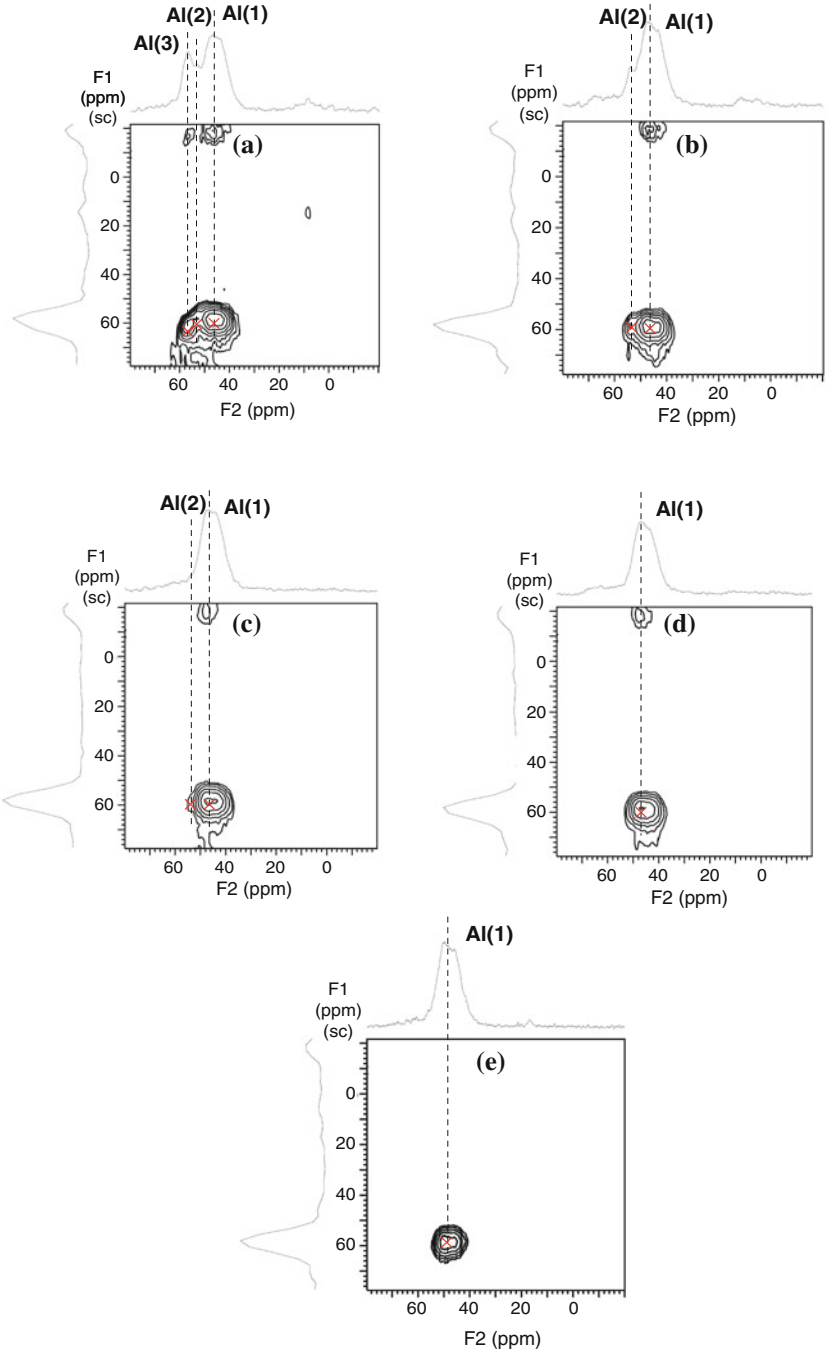

Fig. 4.16 Two-dimensional 3QMAS ^{27}Al-NMR spectra of **a** fresh Fe-zeolite SCR catalysts and samples aged at **b** 650, **c** 750, and **d** 850 °C, and **e** A cordierite spectrum was also recorded since it was present in each of the samples

the aged samples. As the zeolite structure collapses, active cations are freed and they can form oxide clusters such as Fe_2O_3. As the zeolite structure begins to decompose, the surface area decreases, and there will be fewer available sites to bind the Fe cations, and thus the Fe_2O_3 phase will become more prevalent [14]. These results, especially combined with the performance evaluation, point to this zeolite failing when aged above 750 °C. The obvious Fe_2O_3 peak at 54° combined with the drop in surface area of the 850 °C-aged samples provide very strong evidence for zeolite collapse.

Solid-state ^{27}Al-NMR is sensitive to the local structure and bonding and provides a method to extend our description of aluminum bonding in these heterogeneous, amorphous materials [61]. In particular, the 2D experiment that employs triple quantum excitation/evolution and magic angle spinning (3QMAS) has shown great promise in resolving multiple tetrahedral and octahedral aluminum sites as well as penta-coordinate aluminum in zeolites [62]. The suite of stacked ^{27}Al MAS spectra in Fig. 4.15 are of the fresh Fe-zeolite/cordierite samples in the fresh state (a), and after aging at 650 (b), 750 (c), and 850 °C (d), as well as a cordierite blank (e). The same sample suite yields the 3QMAS spectra shown in Fig. 4.16. In both figures, the catalyst spectra are also compared with the spectrum of the cordierite support. Cordierite and Fe-zeolite are constructed of aluminum with tetrahedral coordination represented by the asymmetric resonance band centered at 50 ppm in the 1D spectrum (see Fig. 4.15). The number of distinct aluminum sites is difficult to assess from the 1D data. The 2D spectrum of the fresh Fe-zeolite/cordierite, Fig. 4.16a, clearly shows the broad tetrahedral resonance contains three partially resolved resonances. The Al(1) resonance is due to the support (see Fig. 4.16e). The Al(2) and Al(3) resonances near 55 ppm arise from the Fe-zeolite catalyst [63]. These signals diminish in the successively aged samples, as seen in both Figs. 4.15 and 4.16, and completely disappear in the 850 °C-aged sample. The loss of the signal is attributed to dislodgement of lattice aluminum species to extra-framework positions, perhaps yielding undefined resonances due to the presence of paramagnetic iron species.

Combining all of these characterization techniques and comparing the results to the performance data, it is clear that heating to 850 °C has the most significant impact on the structure and reactivity of the catalysts. These losses in zeolite structure are occurring at lower temperatures compared to the Cu-zeolite (CHA) discussed above [52], but this is essentially due to the difference in zeolite being used. To date there has not been a commercially produced catalyst that has demonstrated the ability to exchange Fe in the CHA zeolite, but there have been some recent academic reports that suggest it is possible and could lead to more thermally durable Fe-zeolite SCR catalysts [64, 65].

The materials characterization is clearly important to help understand and quantify some of the deactivation mechanisms occurring; however, it is not sufficient to explain the deactivation of the front section of the Fe-zeolite SCR, especially the one aged at 650 °C. For this, it is necessary to point to the findings of Jen et al. [35, 36], who illustrated that Pt and to a lesser extent Pd can volatize from the upstream DOC and deposit on the front face of the SCR. This has a deleterious

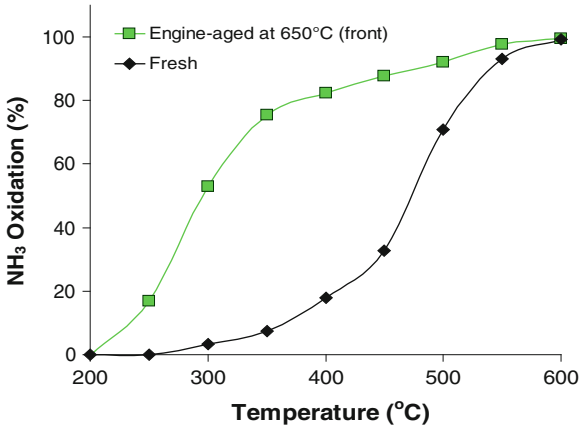

Fig. 4.17 NH_3 oxidation evaluated with 5 % CO_2, 5 % H_2O, 14 % O_2, 350 ppm NH_3, N_2 balance, and a GHSV = 30,000 h^{-1}

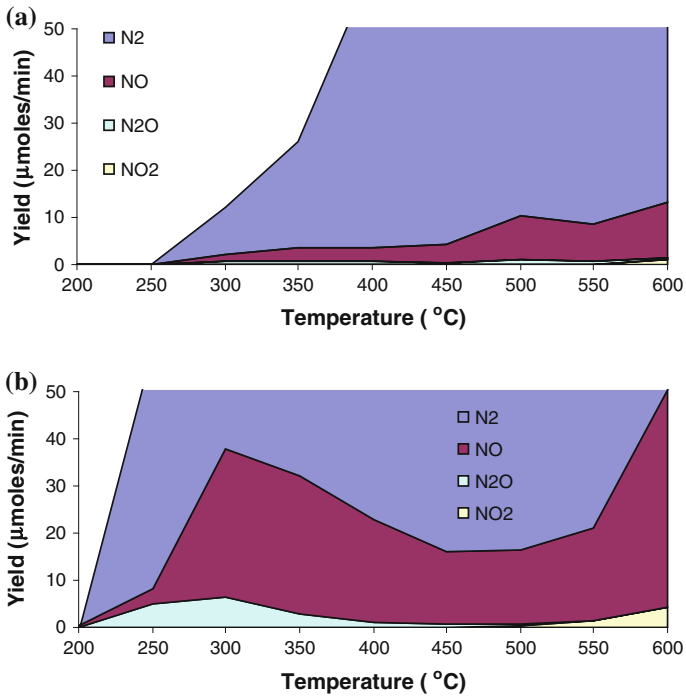

Fig. 4.18 Product yield during the NH_3 oxidation evaluation depicting N_2, NO, N_2O, and NO_2 in **a** fresh SCR catalyst and **b** SCR catalyst engine-aged at 650 °C

effect on NH_3 availability for NO_x SCR as it is easily oxidized over even trace quantities of Pt and Pd. This is clearly illustrated in Fig. 4.17 as the front of the 650 °C-aged sample shows NH_3 oxidation readily occurs above 250 °C, such that above 300 °C less than 80 % of the introduced NH_3 is available. This is coincident with the dramatic decrease in activity shown in Fig. 4.12. Furthermore, with PGM contamination it is expected that the amount of N_2O being made will increase with these catalysts, and Fig. 4.18 illustrates this rise in N_2O yield when comparing the fresh to the 650 °C-aged catalyst. Of course this deactivation mechanism is not unique to Fe-zeolites, and should be a consideration for each NH_3-SCR-based system. Also to be considered are the findings of the follow-up study illustrating the reduced volatilization that occurs with Pt/Pd mixtures [36].

4.5 Summary

As is illustrated in this chapter, Fe-zeolites have a specific role in NH_3-based SCR of NO_x, and provide reaction characteristics that are different from other SCR-based systems. Through application of an appropriate experimental protocol, it is possible to gain deep insight into the detailed workings of these catalysts. Although the chemistry is largely similar to that of Cu-zeolite SCR catalysts, there are key differences that differentiate the two systems:

- The operating window of Fe-zeolite is considerably higher, which is primarily attributed to its decreased activity for NH_3 oxidation by O_2. This is one of the key differentiating attributes of the catalyst, and allows emissions control developers more flexibility when designing their systems. Additionally, a carefully designed system combining with Cu-zeolites and Fe-zeolites could allow a broader temperature window [66–68].
- The NH_3 storage capacity of Fe-zeolite is significantly lower than Cu-zeolite. While this feature is less desirable in a hybrid LNT + SCR system where NH_3 is generated over the LNT and stored on the SCR for later use, it can be preferred from a controls standpoint since there is less accumulation to account for on the catalyst. In fact, the very high storage of NH_3 at low temperatures significantly complicates the functionality of a Cu-only system during transient operation.
- Current model Fe-zeolites have shown hydrothermal stability up to 670 °C, but at higher temperatures there are significant concerns with durability. With further improvements in the zeolite framework, a durable Fe-SCR catalyst may have a role in automotive emissions control of NO_x.

These differences help illustrate the range of catalyst functionality in SCR chemistry, and the protocols outlined here offer guidance on practical methods of

measuring this functionality. Understanding the behavior of the system and how it changes during operation/aging is critically important to implementing and modeling these SCR systems for emissions control, and ultimately improving their functionality and durability.

References

1. U.S. Environmental Protection Agency, "Milestones in Auto Emissions Control", Fact Sheet OMS-12, EPA 400-F-92-014 (1994).
2. W.B. Williamson, J. C. Summers, J.A. Scaparo, ACS Symposium Series, 495 (1992) 26.
3. H. Tamaura, K. Tanaka, Langmuir 10:12 (1994) 4530.
4. W. Grunert, H. Papp, C. Rottlander, M. Baerns, Chemishe Technik 47:4 (1995) 205.
5. U.S. Environmental Protection Agency, Federal Register 70:133 (2005) 40420.
6. X. Feng and W. K. Hall, J. Catal. 166 (1997) 368.
7. M. Koebel, M. Elsener, and M. Kleemann, J. Catal. 180 (1998) 171.
8. H.Y. Chen, and W.M.H. Sachtler, Catal. Lett. 50 (1998) 125.
9. H.Y. Chen, and W.M.H. Sachtler, Catal. Today 42 (1998) 73.
10. R.M. Heck, Catal. Today 53 (1999) 519.
11. R.Q. Long and R.T. Yang, J. Catal., 188 (1999) 332.
12. M. Koebel, M. Elsener, and M. Kleemann, Catal. Today 59 (2000) 33.
13. Q. Sun, Z.X. Gao, H.Y. Chen, and W.M.H. Sachtler, J. Catal. 201 (2001) 89.
14. R.Q. Long and R.T. Yang, Catal. Lett. 74 (2001) 201.
15. R.Q. Long and R.T. Yang, Catal. Lett. 207 (2002) 224.
16. B.R. Wood, J.A. Reimer, and A.T. Bell, J. Catal., 209 (2002) 151.
17. G. Cavataio, J. Girard, J.E. Patterson, C. Montreuil, Y. Cheng, C.K. Lambert, SAE Technical Paper Series 2007-01-1575 (2007) 1.
18. J.R. Theis, SAE Technical Paper Series 2008-01-0811 (2008) 1.
19. Manufacturers of Emission Controls Association, "Emission Control Technology for Stationary Internal Combustion Engines", Status report (1997) 1.
20. U.S. Environmental Protection Agency, "Summary of NOx Control Technologies and their Availability and Extent of Application", EPA 450/3-92-004 (1992).
21. D.M. Chapman, Applied Catalysis A: General 392:1–2 (2011) 143.
22. S. Hu, J.D. Herner, M. Schafer, W. Roberston, J.J. Schauer, H. Dwyer, J. Collins, T. Huai, A. Ayala, Atmos. Environ. 43 (2009) 2950.
23. Z.G. Liu, N.A. Ottinger, C.M. Cremeens, SAE Technical Paper Series 2012-01-0887 (2012) 1.
24. S. Brandenberger, O. Kröcher, A. Tissler, R. Althoff, Catal. Rev. Sci. Eng. 50 (2008) 492.
25. S. Brandenberger, O. Kröcher, A. Tissler, R. Althoff, Appl. Catal. B 95 (2010) 348.
26. S. Brandenberger, O. Kröcher, A. Tissler, R. Althoff, Appl. Catal. A 373 (2010) 168.
27. A. Grossale, I. Nova, E. Tronconi, Catalysis Today 136:1–2 (2008) 18.
28. M. Colombo, I. Nova, E. Tronconi, Catalysis Today 151:3–4 (2010) 223.
29. A. Grossale, I. Nova, E. Tronconi, Catalysis Letters 130:3–4 (2009) 525.
30. A. Grossale, I. Nova, E. Tronconi, J. Catal. 265:2 (2009) 141.
31. M.P. Ruggeri, A. Grossale, I. Nova, E. Tronconi, H. Jirglova, Z. Sobalik, Catal. Today 184:1 (2012) 107.
32. Y. Cheng, C. Montreuil, G. Cavataio, C.K. Lambert, SAE Technical Paper Series 2008-01-1023 (2008) 1.
33. G. Cavataio, H.-W. Jen, J.R. Warner, J.W. Girard, J.Y. Kim, C.K. Lambert, SAE Technical Paper Series 2008-01-1025 (2008) 1.
34. V.Y. Prikhodko, J.A. Pihl, S.A. Lewis, J.E. Parks, SAE Technical Paper Series 2012-01-1080 (2012) 1.

35. H.W. Jen, J.W. Girard, G. Cavataio, and M.J. Jagner, SAE Technical Paper Series 2008-01-2488 (2008).
36. G. Cavataio, H.W. Jen, J.W. Girard, and M.J. Jagner, SAE Technical Paper Series 2009-01-0627 (2009).
37. T. J. Toops, K. Nguyen, A.L. Foster, B.G. Bunting, N.A. Ottinger, J.A. Pihl, E.W. Hagaman, J. Jiao, Catal. Today 151 (2010) 257.
38. R.G. Silver, M.O. Stefanick, B.I. Todd, Catal. Today 136:1–2 (2008) 28.
39. J. Li, R.H. Zhu, Y.S. Cheng, C.K. Lambert, R.T. Yang, Environmental Science & Technology 44:5 (2010) 1799.
40. L. Ma, J. Li, Y.S. Cheng, C.K. Lambert, L.X. Fu, Environmental Science & Technology 46:3 (2012) 1747.
41. S. Brandenberger, O. Kröcher, Chimia 66 (2012) 687.
42. A. Grossale, I. Nova, E. Tronconi, D. Chatterjee, M. Weibel, J. Catal. 256:2 (2008) 312.
43. P.S. Metkar, V. Balakotaiah, M.P. Harold, Catalysis Today 184:1 (2012) 115.
44. L. Olsson, H. Sjovall, R.J. Blint, Appl. Catal. B 81:3–4 (2008) 203.
45. J.A. Pihl, "Development of a CLEERS transient experimental protocol for urea/ammonia SCR", 2010 DOE Crosscut Workshop on Lean Emissions Reduction Simulation (CLEERS), Dearborn, MI, USA, April 20, 2010.
46. K. Kamasamudram, N.W. Currier, X. Chen, A. Yezerets, Catalysis Today 151 (2010) 212.
47. H. Sjövall, R.J. Blint, A. Gopinath, L. Olsson, Ind. Eng. Chem. Res. 49 (2010) 39.
48. A. Schuler, M. Votsmeier, P. Kiwic, J. Geisshoff, W. Hautpmann, A. Drochner, H. Vogel, Chem. Eng. J. 154:1–3 (2009) 333.
49. M. Colombo, I. Nova, E. Tronconi, V. Schmeisser, B. Bandl-Konrad, L. Zimmerman, Appl. Catal. B: Environ. 111 (2012) 106.
50. G. Madia, M. Koebel, M. Elsener, A. Wokaun, Ind. Eng. Chem. Res. 41:16 (2002) 4008.
51. G. Delahay, S. Kieger, B. Neveu, B. Coq, Comptes Rendus deL Academie des Sciences Serie II Fascicule C-Chimie 1:4 (1998) 229.
52. S.J. Schmieg, S.H. Oh, C.H. Kim, D.B. Brown, J. H. Lee, C.H.F. Peden, D. H. Kim, Catalysis Today 184 (2012) 252.
53. G. Cavataio, H.-W. Jen, D.A. Dobson, J.R. Warner, SAE Technical Paper Series 2009-01-2823 (2009) 1.
54. D.W. Brookshear, K. Nguyen, T. J. Toops, B.G. Bunting, J. Howe, Catalysis Today 184 (2012) 205.
55. D.W. Brookshear, K. Nguyen, T. J. Toops, B.G. Bunting, Topics in Catalysis 56:1–8 (2013) 62.
56. A. Williams, J. Burton, R.L. McCormick, T.J. Toops, A.A. Wereszczak, E.E. Fox, M.J. Lance, G. Cavataio, D. Dobson, J. Warner, R. Brezny, D.W. Brookshear, K. Nguyen, SAE Technical Paper Series 2013-01-0513 (2013) 1.
57. M. Devadas, O. Krocher, A. Wokaun, React. Kin. Catal. Lett. 86:2 (2005) 347.
58. M. Devadas, O. Krocher, M. Elsener, A. Wokaun, G. Mitrikas, N. Soger, M. Pfeifer, Y. Demel, L. Mussmann, Catal. Today 119:1 (2007) 137.
59. K. Rahkamaa-Toloen, M.L. Maunula, M. Huuhtanen, R.L. Keiski, Catal. Today 100:3–4 (2005) 217.
60. N.A. Ottinger, K. Nguyen, B.G. Bunting, T.J. Toops, J. Howe, SAE International Journal of Fuels and Lubricants 2:1 (2009) 217.
61. M. E. Smith, Appl. Magn. Reson. 4 (1993) 1.
62. J. Huang, Y. Jiang, V. R. R. Marthala, B. Thomas, E. Romanova, M. Hunger, J. Phys. Chem. C 112 (2008) 3811.
63. J. Perez-Ramirez, J. C. Groen, A. Bruckner, M. S. Kumar, U. Bentrup, M. N. Debbagh, and L. A. Villaescusa, J. Catal. 232 (2005) 318.
64. Q. Ye, L. Wang, R.T. Yang, Appl. Catal. A 427–428 (2012) 24.

65. X.F. Yang, Z.L. Wu, M. Moses-Debusk, D.R. Mullins, S.M. Mahurin, R.A. Geiger, M. Kidder, C.K. Narula, J. Phys. Chem. C 116:44 (2012) 23322.
66. P.S. Metkar, M.P. Harold, V. Balakotaiah, Chem. Engr. Sci. 87 (2013) 51.
67. Y. Liu, M.P. Harold, D. Luss, Appl. Catal. B 121 (2012) 239.
68. P.S. Metkar, M.P. Harold, V. Balakotaiah, Appl. Catal. B 111 (2012) 67.